Materials Science & Engineering A 972 (2026) 150666

Contents lists available at ScienceDirect

Materials Science & Engineering A

journal homepage: www.elsevier.com/locate/msea

Characterizing the influence of weld time on the Fe-Zn interface during liquid metal embrittlement of resistance spot welded TWIP steel

Gautham Mahadevan [a,*], Virginia Bertolo [a], Soheil Sabooni [c], He Gao [c], Vera Popovich [a], Leo A.I. Kestens [a,b], Marcel Hermans [a]

[a] Department of Materials Science and Engineering, Delft University of Technology, Mekelweg 2, Delft, 2628 CD, the Netherlands
[b] Department of Electromechanics, Systems and Metals Engineering, Ghent University, Technologiepark 46, Gent, 9052, Belgium
[c] Tata Steel Nederland Technology B.V., P.O. Box 1000, IJmuiden, 1970 CA, the Netherlands

ARTICLE INFO

Keywords:
Liquid metal embrittlement
Resistance spot welding
Zn diffusion
Intermetallics
STEM
EBSD
EDS
TWIP steel
Numerical modelling

ABSTRACT

This study examines how weld time (WT) influences the Fe–Zn interface and liquid metal embrittlement (LME) during resistance spot welding (RSW) of electrogalvanized TWIP steel. Eight weld times ranging from 300 ms to 1700 ms were investigated under constant welding parameters. At 300 ms, the Zn coating remained intact with no intermetallic (IM) phases detected. At 500 ms, continuous layers of δ, Γ, and α-Fe(Zn) phases formed at the weld shoulder, confirmed by SEM-EDS, STEM-EDS, and EBSD, with α-Fe(Zn) showing Al enrichment and Mn depletion. At 700 ms, initial LME cracks appeared, accompanied by fragmented IM layers. For weld times between 900 ms and 1700 ms, crack width and depth increased significantly (from ∼21 μm to ∼490 μm), while IM phases were absent. Finite element analysis (FEA) simulations of temperature distribution correlated with experimental observations: IM formation occurred within the predicted stability range at 500 ms, became discontinuous at 700 ms, and disappeared at higher weld times as local temperatures exceeded 800 °C. These results demonstrate that IM formation precedes LME crack initiation and that prolonged weld time accelerates IM breakdown and crack propagation. The findings provide a mechanistic link between thermal conditions, interfacial reactions, and LME severity, offering guidance for optimizing RSW parameters in automotive applications.

1. Introduction

In automotive manufacturing, reducing fuel consumption and lowering vehicle weight without compromising on strength or crash resistance has been a major objective in recent decades to improve the overall carbon footprint [1]. Advanced high-strength steels (AHSS) provide both high strength and elongation, making them suitable for automotive applications [2–4]. Resistance spot welding (RSW) is the primary joining technique in automotive manufacturing, with 3000 to 5000 spot welds typically present in each vehicle. In RSW, a weld joint is formed by the combined effect of electrode force and Joule heating produced by melting and solidification that leads to the formation of a weld nugget. The process is controlled through parameters including electrode force, electrode geometry, welding current, squeeze time, weld time, and hold time. Each RSW cycle consists of three stages. In the first stage called 'squeeze time', an electrode force is applied on the steel sheets in the absence of welding current. This is followed by the 'weld time (WT)', during which the force is maintained while current is applied to form the spot weld. Finally during the 'hold time', the electrode force is maintained by water-cooled electrodes in the absence of welding current [5,6]. The temperature and stress generated during RSW can allow liquid Zn to penetrate into the steel substrate, leading to the formation and propagation of cracks. This phenomenon, known as liquid metal embrittlement (LME), is a major concern for AHSS such as twinning-induced plasticity (TWIP) steels, since every weld can act as a failure site [7]. Multiple studies show TWIP steels are highly susceptible to LME despite their strength and ductility, due to their austenitic microstructure being particularly susceptible to embrittlement [8–12]. LME mechanisms are not yet fully understood because crack initiation and propagation depend on the combined effects of stress, temperature, strain, and steel microstructure. The local variations in stress, temperature, and microstructure across a weld further increase this complexity and result in different types of LME cracks forming in different regions of the weld [7]. Several theories have been suggested to explain the micro-mechanisms of LME, which depend on the specific solid/liquid metal pair. In the Fe-Zn system, stress-assisted GB diffusion is considered

* Corresponding author.
E-mail address: g.mahadevan@tudelft.nl (G. Mahadevan).

https://doi.org/10.1016/j.msea.2026.150666
Received 5 January 2026; Received in revised form 8 June 2026; Accepted 23 June 2026
Available online 24 June 2026

to be the dominant micro-mechanism [13,14]. Most stress-assisted LME models are based on the Rehbinder effect, where Zn diffuses into the steelGBs, lowers the steel surface energy, and causes embrittlement once a critical stress is reached [14–16].

Fe-Zn intermetallics (IM) play an important role at controlling LME at the interface of the steel substrate and Zn coating during RSW. When the Zn coating is subjected to temperatures above 427 °C under electrode force, it reacts with Fe to form IM compounds. The presence, thickness, and stability of these compounds determine how Zn is transported and how it remains available at the interface [17–21]. According to Murugan et al., at 700 °C the δ ($FeZn_{10}$) phase in the interface coating transforms into liquid Zn and Γ (Fe_3Zn_{10}). Under these conditions, Γ is not stable with Fe, leading to the formation of a thin Zn-rich ferritic (α-Fe(Zn)) layer as Zn diffuses into Fe. Zn redistribution between α-Fe(Zn), Γ, and liquid Zn continuously re-establishes equilibrium, with Zn ultimately moving from the liquid phase through Γ into the steel [22]. Lee et al. reported that an Al-rich diffusion-inhibiting layer suppresses the formation of Fe-Zn IM at the Zn/steel interface, but this layer is destroyed during RSW due to heat and electrode stress. In cracked regions, fine α-Fe(Zn) particles appear on the steel surface and cracks propagate along austenite grain boundaries beneath this layer [23]. The crack area consists of Γ and α-Fe(Zn), showing that Zn infiltrates grain boundaries. The α-Fe(Zn) particles increase interfacial area and act as brittle phases, providing pathways for Zn infiltration and thereby accelerating LME, which becomes more severe with higher welding current [22]. Additionally, Al enrichment zones at the Fe-Zn interface have been observed in previous studies. This Al-rich interfacial region acts as a diffusion barrier between the Zn coating and the steel substrate [24–26]. When Fe-Zn IMs at the coating-steel interface break down, Zn from the coating is available to diffuse into the GBs of the substrate. Ikeda et al. reported that in grain boundaries infiltrated with Zn but not yet cracked, a nanoscale Γ phase could be characterized. The observation of this phase indicates that strain heterogeneities are locally enhanced within the grain boundary network, and IM formation does not occur only after cracks develop and liquid Zn penetrates, but instead acts as a primary nanoscale factor that weakens grain boundaries and promotes crack initiation [27].

Although different Fe-Zn IM phases have been reported in studies where welding current was varied, the true sequence of events before, during, and after IM formation at the weld interface has not been studied in detail. Furthermore, no previous study has combined high resolution Fe-Zn interface characterisation with a validated FEA model to explain IM formation and breakdown during LME in RSW. Additionally, while weld current has been widely studied, the effect of weld time has received little attention. While prior studies have characterized Fe-Zn interface under Gleeble testing conditions or under limited RSW conditions, the evolution of the Fe-Zn interface from pre-IM formation through crack initiation and propagation as a function of a RSW heat input has not been established. Furthermore, a direct quantitative link between the local thermal history at LME-sensitive regions and the experimentally observed IM phases has not been reported. This study addresses these gaps in LME literature. Increasing the weld time not only increases the temperature in the nugget and shoulder (area adjacent to the electrode) regions but also influences the diffusion kinetics that govern IM formation and stability [28–31]. The effect of weld time on these processes is not well understood, leaving a gap in knowledge about the evolution of the Fe-Zn interface during RSW. In this study, eight welding conditions with WT from 300 ms to 1700 ms were studied, and the Fe-Zn interface evolution was characterized, while keeping all other welding parameters constant. The aim of the study is to capture the evolution of the Fe-Zn interface at the weld shoulder: before IM formation, during IM formation, crack initiation and crack growth. The weld shoulder was selected because LME cracks consistently initiate in this region due to the availability of liquid Zn and favourable stress and temperature conditions [32]. Furthermore, an FEA simulation of the RSW process with the same materials, weld setup and parameters was run to validate the experimental observations and provide a complete picture of the Fe-Zn interface during RSW.

2. Material and methods

2.1. Materials

The steel grade in this study was a 1.23 mm thick, electro-galvanized, cold-rolled austenitic TWIP steel. During RSW, this TWIP sheet was placed on top of two DX54 steel sheets of thickness 1.5 mm each to form a heterogeneous triple-layer stack, as illustrated in Fig. 1. The triple-layer configuration and use of DX54 steel were chosen to increase the stress concentration and heat input, which are conducive to LME crack formation [18]. The concentrations of the primary alloying elements in the TWIP steel are listed in Table 1. The composition of the DX54 sheet is given in Table 2.

2.2. Welding setup

Resistance spot welding was carried out using a 1000 MHz MFDC spot welding machine with constant current control. ISO5821 F1-16-20-6 CuCr1Zr electrodes were tip-dressed prior to welding. The welding current, electrode force, squeeze time, and hold time settings are specified in Table 3. A total of eight weld times were selected, ranging from 300 ms to 1700 ms in 200 ms increments. The parameters were optimized such that no expulsion was observed at WT = 1700 ms. Four samples were produced for each welding condition to ensure reproducibility and statistical reliability.

2.3. Characterization

A VHX7000N optical microscope was employed to locate LME cracks on the surface of the spot welds. These identified crack regions were then selected for cross-sectional analysis. For SEM preparation, the cross-sections were ground with progressively finer grit sandpapers and polished sequentially using 3 μm silica paste followed by 1 μm diamond paste and OP-S liquid to obtain a smooth surface suitable for imaging. Scanning electron microscopy (SEM) was carried out using a JEOL®

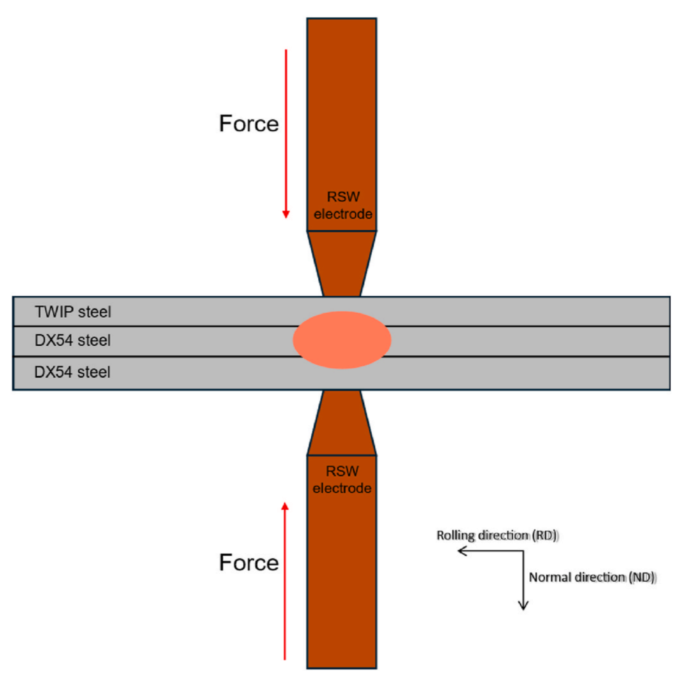

Fig. 1. Schematic representation of the RSW setup showing the sample coordinate system.

Table 1
Composition of alloying elements in TWIP steel in wt%.

Mn	Al	C	Ni
17.3	1.49	0.61	0.36

Table 2
Composition of alloying elements in DX54 steel in wt%.

C	Si	Mn	P
0.12	0.5	0.6	0.1

Table 3
RSW process parameters.

Weld current (kA)	Electrode force (kN)	Squeeze time (ms)	Hold time (ms)	Weld time (WT) (ms)
7.4	4.5	150	150	**300, 500, 700, 900, 1100, 1300, 1500, 1700**

IT800SHL™ equipped with a field emission gun, operating at 10 kV and a beam current of 3.2 nA. The system was also equipped with an Oxford Instruments® Maxim 100™ detector to perform Energy Dispersive Spectroscopy (EDS) and.

Electron Backscatter Diffraction (EBSD) for microstructural analysis. X-ray diffraction (XRD) analysis was performed using a Bruker D8 Discover diffractometer with an Incoatec Microfocus Source (IμS) operated at 50 kV and 1000 μA with Cu Kα radiation. Measurements were carried out in continuous θ–2θ mode with a step size of 0.04° and a dwell time of 2 s per step. Data were analysed using Bruker DiffracSuite software. Scanning transmission electron microscopy (STEM) was performed using a JEOL JEM-2200FS Cs-corrected microscope operated at 200 kV, equipped with a Schottky field-emission gun (FEG) and a JEOL JED-2300D EDX system. Electron transparent lamellae were prepared by the conventional lift-out method using a Helios G4 PFIB UXe xenon plasma focused ion beam (FIB). To protect the interface features from ion milling damage, a thin layer of platinum was deposited by beam-induced deposition prior to thinning. The parameters to extract STEM lamellae using FIB were obtained from Krenn et al. [33].

2.4. FEA simulation

FEA simulations were performed using SORPAS to model the RSW process and estimate the temperature distribution across the weld. The simulation setup replicated the experimental RSW configuration, using the same material properties of the sheets, electrode geometry, coating conditions, and thicknesses as the actual spot welds. The thermo-mechanical properties of the steel sheets were obtained from JMatPro [34]. The simulations were performed at weld times of 500 ms, 700 ms, and 900 ms to correspond with the experimental conditions. Fig. 2 shows the weld simulation mesh used in SORPAS. The main objective of the simulations was to determine the temperature distribution at different regions of the weld, particularly near the Fe-Zn interface, to validate experimental observations.

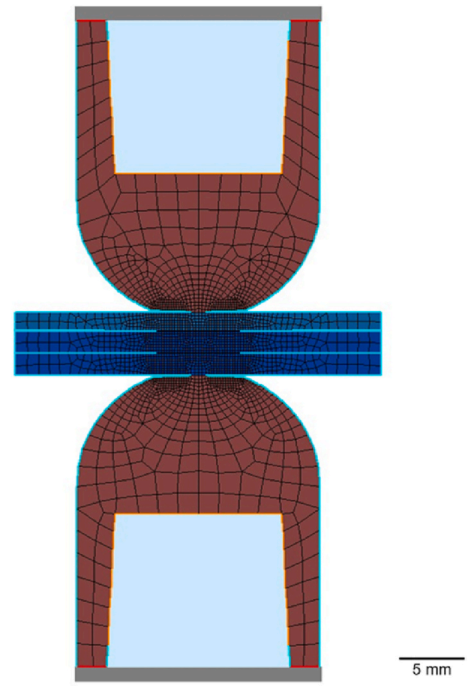

Fig. 2. RSW FEA setup to calculate temperature distribution.

3. Results

3.1. Microstructure characterisation of LME cracks

SEM analysis of the RSW joints (Fig. 3) shows the evolution of the Fe-Zn interface with increasing weld time. At 300 ms, the Zn coating and interface remained intact, with no visible damage. At 500 ms, no LME cracks were observed, but the Zn layer showed local break-up and pore formation. At 700 ms, the first LME cracks appeared at the weld shoulder, consistent with Type B intergranular cracks. As the weld time was increased to 900 ms, 1100 ms, 1300 ms, 1500 ms and 1700 ms, the severity of embrittlement was observed to increase. LME severity was quantified by measuring the width and depth of cracks. Since Fe-Zn IM formation and crack initiation occur between 300 ms and 700 ms, most characterization in this study was focused on this weld time range.

The crack depth and width from all samples at each weld parameter were averaged. Both the average depth and width showed the same increasing trend with weld time, as shown in Fig. 4. The average crack depth was ~21 μm at 700 ms and increased to ~32 μm at 900 ms. As the weld time increased to 1100 ms, the depth reached ~60 μm. As the weld time was increased further, a larger increase was observed in crack depth, reaching ~125 μm, ~220 μm, and ~490 μm at 1300 ms, 1500 ms, and 1700 ms, respectively. Similar trends were observed for crack width, with an average length of ~2 μm at a weld time of 700 ms, and increasing to an average width of ~57 μm at the highest weld time of 1700 ms. The Zn coating thickness was measured both on regions away from the weld and in the weld shoulder. The Zn coating away from the weld was measured to be between 5 and 10 μm, consistent with typical electrogalvanized coatings [4]. In the weld shoulder region, the coating thickness increased to 15-25 μm due to the accumulation of liquid Zn, because the electrode force drives molten Zn outward from the weld centre.

3.2. Fe-Zn interface characterization

In this section, welds produced at 300 ms, 500 ms and 700 ms are studied in further detail. The characterization focuses on the weld shoulder region, and results from SEM, EDS and EBSD are presented. These characterization techniques are used to identify the phases present at the Fe-Zn interface and to describe the elemental distribution in and around the interface at different weld times. From the composition of the steel used, the Fe-Zn phase diagram as well as other studies on the Fe-Zn interface [33], the possible phases present in the interface is listed in Table 4.

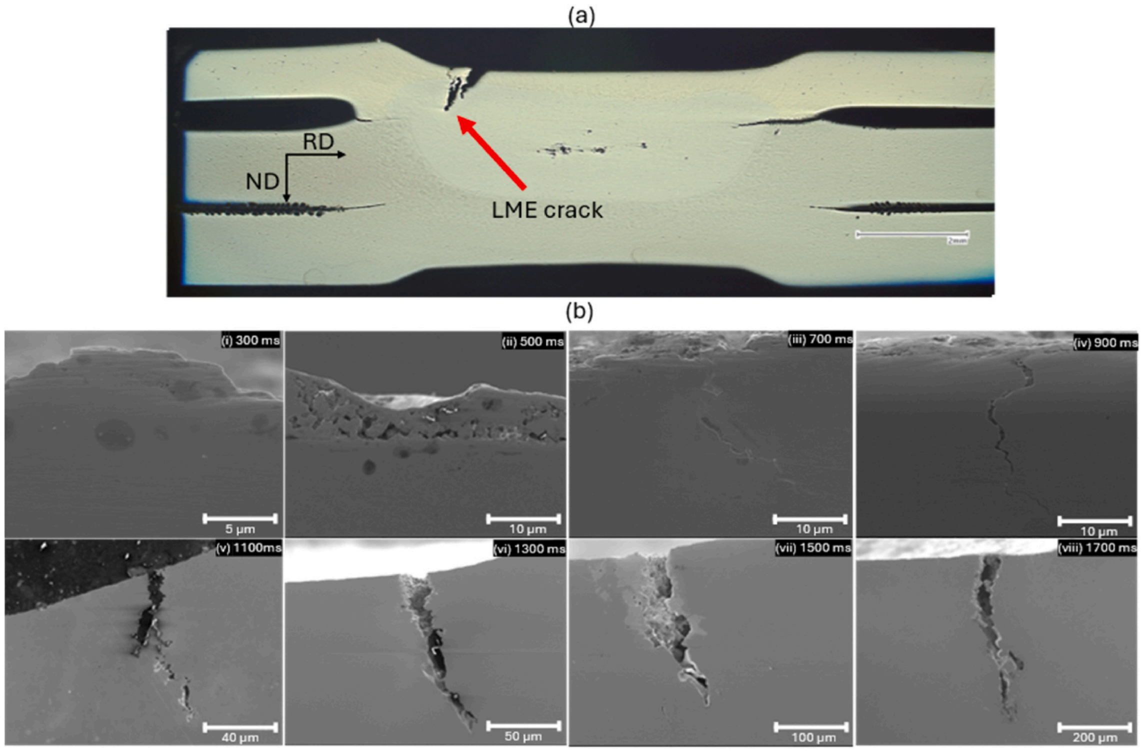

Fig. 3. (a) Representative optical micrograph of weld cross-section at WT = 1700 ms showing an LME crack (b) SEM micrographs of RSW shoulder region at weld time of (i) 300 ms (ii) 500 ms (iii) 700 ms (iv) 900 ms (v) 1100 ms (vi) 1300 ms (vii) 1500 ms (viii) 1700 ms

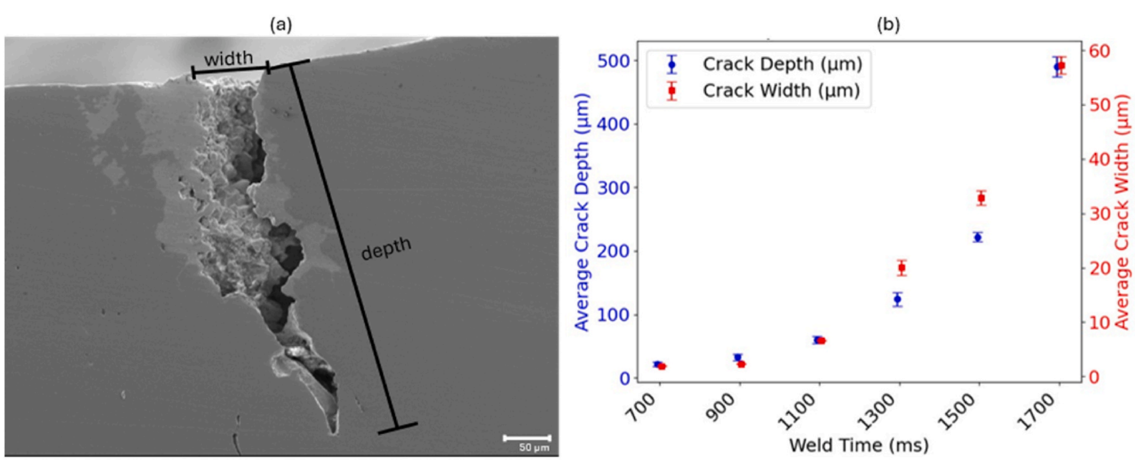

Fig. 4. (a) Schematic diagram for crack dimension measurement (b) Average of 4 samples LME crack depth and crack width at different weld times, error bars indicate one standard deviation.

Table 4
Possible phases present in Fe-Zn interface [33,35].

Phase	Formula	Crystal structure	Temperature range (°C)
α-Fe	α-Fe(Zn)	BCC	<782
Γ	Fe_3Zn_{10}	BCC	~530-665
Γ_1	Fe_5Zn_{21}	FCC	~540-665
δ	$FeZn_{10}$	HCP	~530-782
ζ	$FeZn_{13}$	monoclinic	~430-530

3.2.1. WT = 300 ms

At a weld time of 300 ms, the electrogalvanized Zn coating remains intact on the TWIP steel. The steel retains its fully austenitic structure, and no Fe-Zn IM phases can be identified by EBSD, as shown in Fig. 5. Analysis along the weld shoulder shows no evidence of LME cracks. The Zn coating is unindexed by EBSD and appears black in colour.

From the EDS elemental map, three distinct regions can be identified at the interface, as shown in Fig. 5. The average weight percentage of various alloying elements in these regions is measured (Table 5). The uppermost region corresponds to the Zn coating, below which there is an intermediate interface layer that is Fe rich and shows enrichment in Al and depletion of Mn relative to the bulk TWIP steel substrate, which forms the bottommost layer.

3.2.2. WT = 500 ms

At a weld time of 500 ms, no LME crack was observed in the RSW samples. However, multiple IM phases are observed in the weld shoulder region. These phases appear as distinct layers at the Fe-Zn interface. To characterize the phases and their distribution, XRD, SEM-EDS, EBSD and

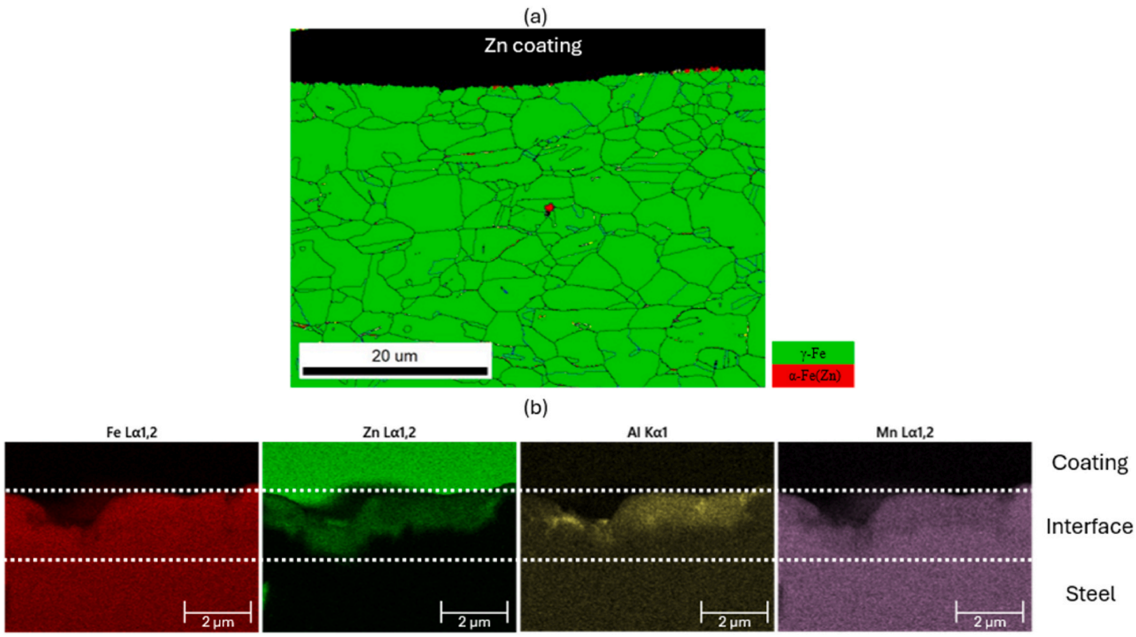

Fig. 5. Characterization of RSW sample at WT = 300 ms showing (a) EBSD phase map of Fe-Zn interface (b) EDS elemental map showing the different layers of the Fe-Zn interface.

Table 5
Average weight percentage of different elements in the coating, interface and steel substrate.

	Fe (wt %)	Zn (wt %)	Al (wt %)	Mn (wt %)
Coating	12.93	78.34	0.23	0.18
Interface	60.91	24.97	4.15	8.37
Steel	75.21	0.47	1.86	17.25

STEM-EDS analyses were performed on this sample. The analysis was performed in the Fe-Zn interface at the weld shoulder region, shown in Fig. 6.

3.2.2.1. XRD. XRD analysis was carried out in the weld shoulder region to identify the phases present. The XRD spectrum is shown in Fig. 7 with the detected phases labelled. Zn, ZnO, δ and Γ were identified from the diffraction peaks. Notably, α-Fe(Zn) and γ-Fe could not be identified by XRD. Due to the similar atomic configurations, Γ and Γ_1 IM phases are not easily distinguishable [35] (see Fig. 8).

3.2.2.2. EBSD. Fig. 8(a) and (b) shows the EBSD phase map of the Fe-Zn interface at two different magnifications of 1500× and 6000x respectively, and indicates the formation of layered Fe-Zn IMs. The δ phase is observed at the top, followed by a layer of Γ. Below this, a continuous chain of α-Fe(Zn) is present at the interface, with austenitic Fe underneath. The α-Fe chain is interspersed with the Γ phase and exhibits an elongated morphology. Although EBSD phase identification characterizes the intermediate layer as α-Fe(Zn), the results need further validation due to potential misindexation during EBSD. Thus, SEM-EDS and STEM were used to validate EBSD characterization. α-Fe(Zn) was identified by its Fe-rich composition (>72 wt% Fe, while Γ was identified by its Zn-rich composition (~73 wt% Zn). This approach is described in detail in the EDS and STEM subsections below.

3.2.2.3. EDS. Elemental mapping and point composition analysis were done to study the distribution of alloying elements at the Fe-Zn interface, as shown in Fig. 9. The elemental maps show Zn-rich IM layers, beneath which an Fe-rich, Zn-poor phase is interspersed within a Zn-rich, Fe-poor phase. The Fe-rich phase, identified as α-Fe(Zn) by EBSD,

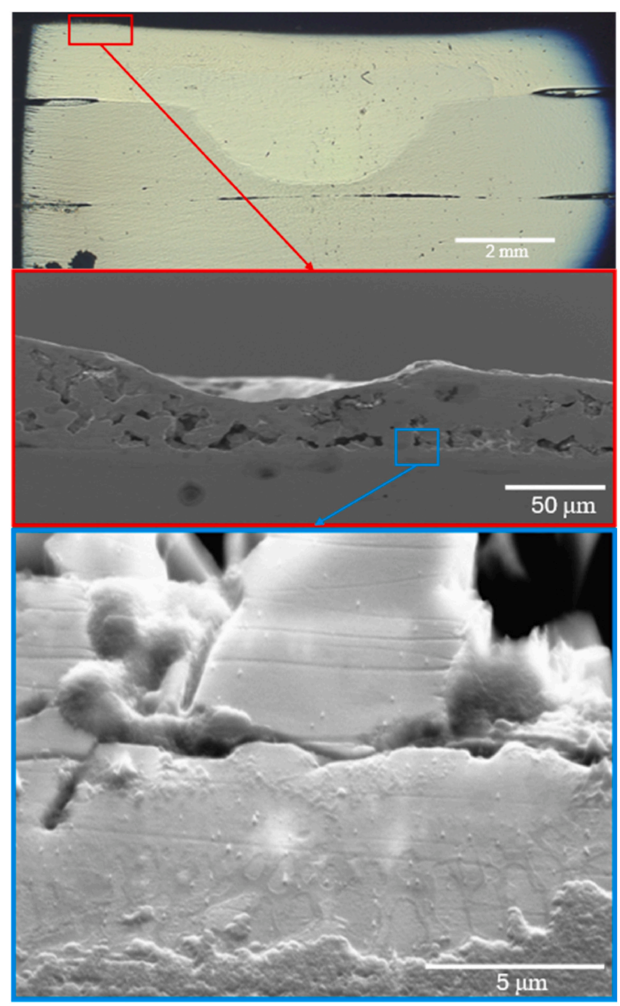

Fig. 6. Analysis area of RSW shoulder Fe-Zn interface for characterization.

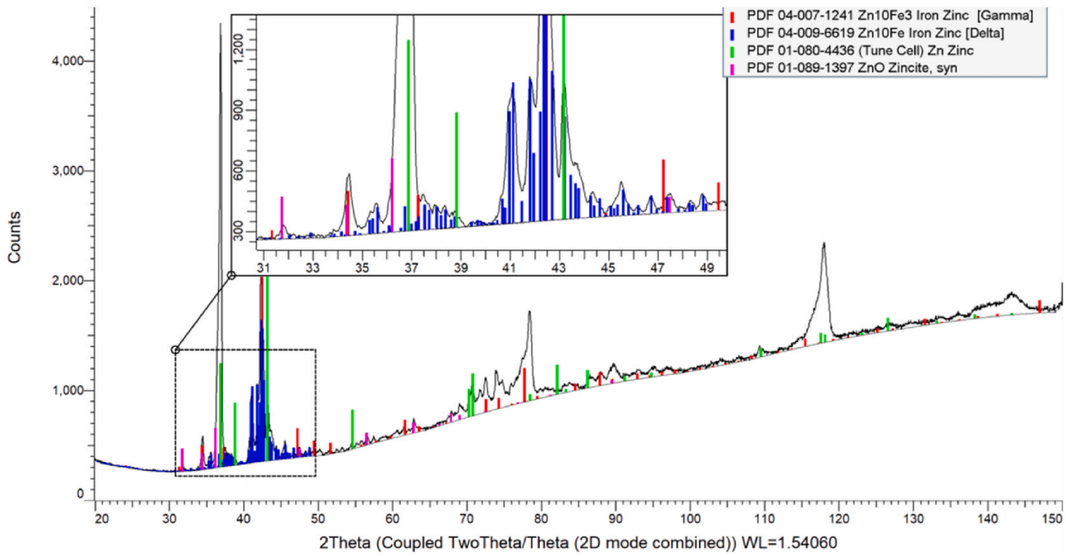

Fig. 7. XRD spectrum from weld shoulder of RSW sample at WT = 500 ms

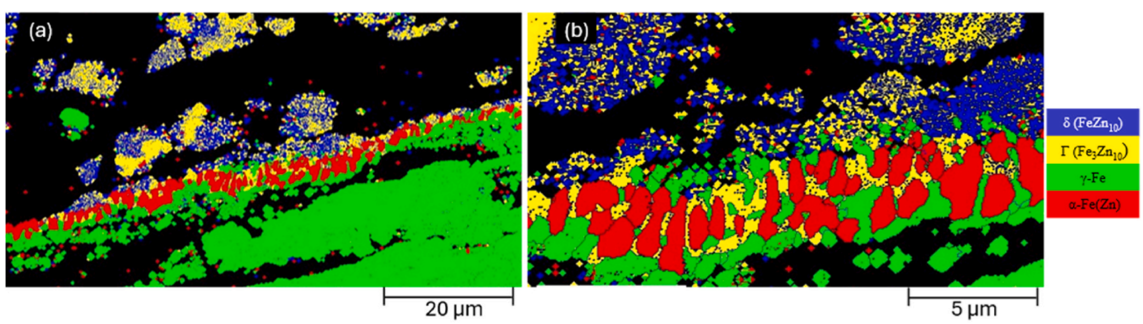

Fig. 8. EBSD phase map of RSW sample at WT = 500 ms at a magnification of (a) 1500× (b) 6000x

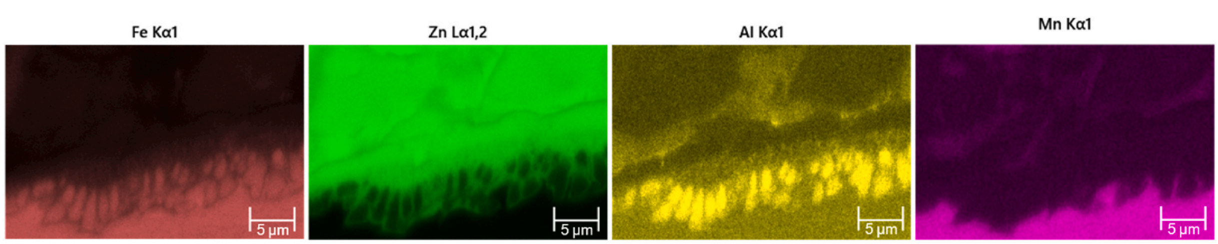

Fig. 9. SEM-EDS map of RSW Fe-Zn interface at WT = 500 ms of alloying elements.

is enriched in Al, with Al concentration higher than in the surrounding steel or IM layers. The same phase also shows Mn depletion compared to the steel substrate, which is confirmed by point analysis. The Fe-rich phase has a composition of 72.06 wt% Fe, 18.92 wt% Zn, 5.91 wt% Al and 2.11 wt% Mn. The region above this phase contains 73.18 wt% Zn, 20.43 wt% Fe, 0.24 wt% Al and 4.67 wt% Mn. Based on composition and phase identification, the Fe-rich phase is most consistent with α-Fe(Zn), while the phase above corresponds to the Γ phase.

3.2.2.4. STEM. STEM analysis was carried out on a lamella extracted from the Fe-Zn interface. The objective of this analysis was to confirm the identity of the BCC phase that EBSD had suggested as α-Fe. STEM-EDS line scans and point elemental analysis were performed to determine the composition of the different phase regions, as shown in Fig. 10.

The STEM-EDS results validate the SEM-EDS observations, showing that a Zn-rich α-Fe layer forms between the austenitic steel and the Fe-Zn IM layers, as shown in Fig. 11. The Fe and Zn weight percentage measured in these grains corresponds stoichiometrically to α-Fe(Zn) [22]. Similarly, the phase surrounding these grains is characterized to be Γ, which forms an uneven interface with the underlying austenitic steel. STEM-EDS elemental mapping further confirms these results, showing a Zn-rich interface containing grains that are relatively poorer in Zn, Al and Mn and enriched in Fe.

3.2.3. *WT = 700 ms*

Characterization of the RSW samples at WT = 700 ms were performed using EDS and EBSD, as shown in Fig. 12. A narrow LME crack is observed at the edge of the weld shoulder. At the crack opening, no IMs or α-Fe(Zn) grains were present. Unlike the continuous layered structure observed at 500 ms, these phases appear discontinuous and fragmented in the 700 ms sample. These results indicate that 700 ms represents the transition stage, where IM layers begin to break down and LME crack

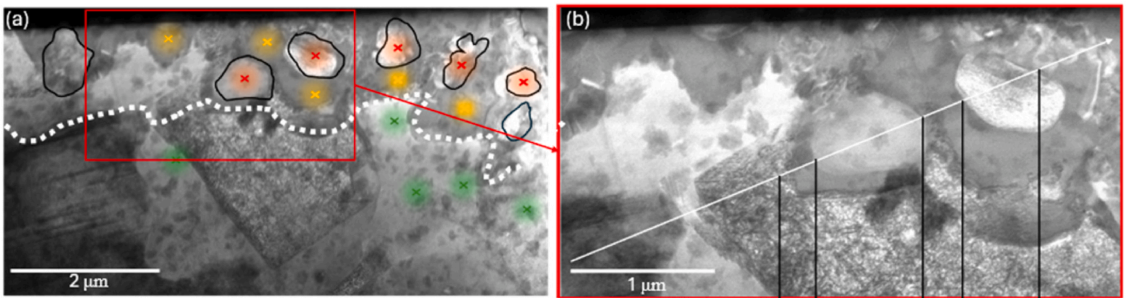

(c)

Marker	Fe wt%	Zn wt%	Al wt%	Mn wt%
× (red)	78.45	18.20	1.85	1.5
× (yellow)	22.91	74.45	0.15	2.48
× (green)	82.08	0.07	0.72	17.13

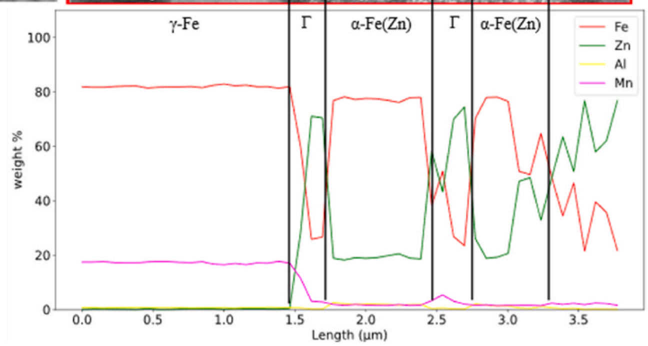

Fig. 10. STEM-EDS analysis of RSW sample at WT = 500 ms showing (a) point analysis to measure elemental distribution of different phases, (b) line scan of Fe-Zn IM phases, (c) weight percentages of various alloying elements from point analysis.

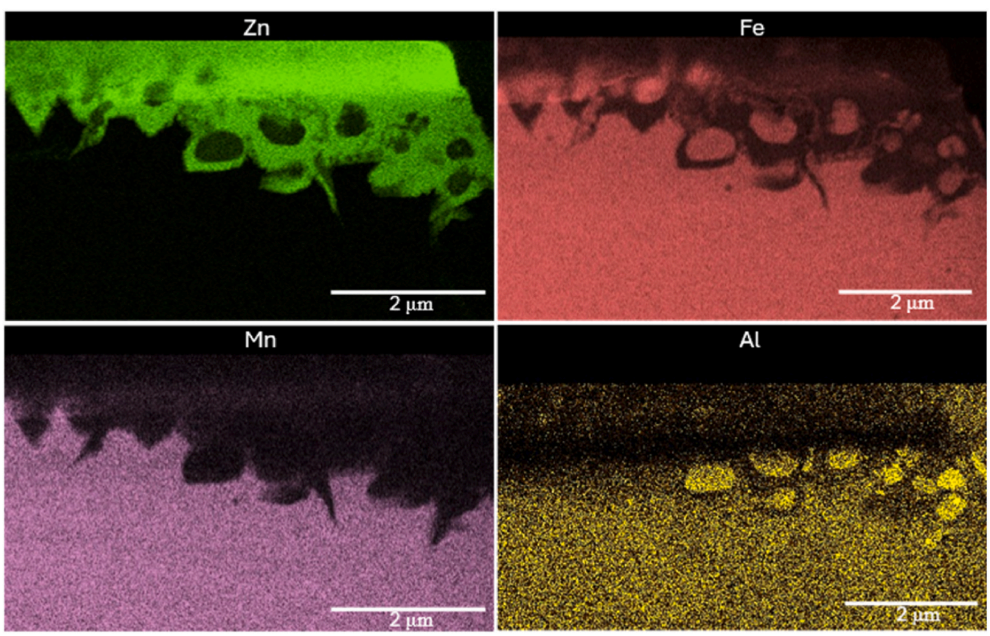

Fig. 11. STEM-EDS map of RSW Fe-Zn interface at WT = 500 ms

formation is observed. Some isolated features are indexed as BCC within some austenite grain interiors. As no change in composition was detected in these regions by SEM-EDS or STEM-EDS, these features are attributed to EBSD phase misindexation.

3.2.4. WT = 900 ms to 1700 ms

Fig. 13 shows the EBSD phase maps obtained from RSW samples with weld times between 900 ms and 1700 ms. LME cracks are present in all samples within this range. No Fe-Zn IM phases were characterized at any of the RSW samples. As shown in Fig. 4, both the depth and width of the LME cracks increase with increasing weld time. At a weld time of 900 ms to 1300 ms, the crack initiates in the shoulder region and all the characterized grains are predominantly austenitic. At weld times of 1500 ms and 1700 ms, the lower part of the crack extends into the weld fusion zone, which is indexed as ferritic. While the crack dynamics and growth in the weld fusion zone are affected by the welding conditions, it is not the focus of this study.

3.3. Comparing FEA and experimental observations

3.3.1. Comparison of weld nugget geometry

To validate the accuracy of the FEA model, the weld nugget areas from the RSW simulation and the experimentally obtained weld cross-sections were compared at weld times of 500 ms, 700 ms, and 900 ms. Fig. 14 shows the comparison between the experimental cross-sections and the simulated weld nuggets, and Table 6 summarizes the

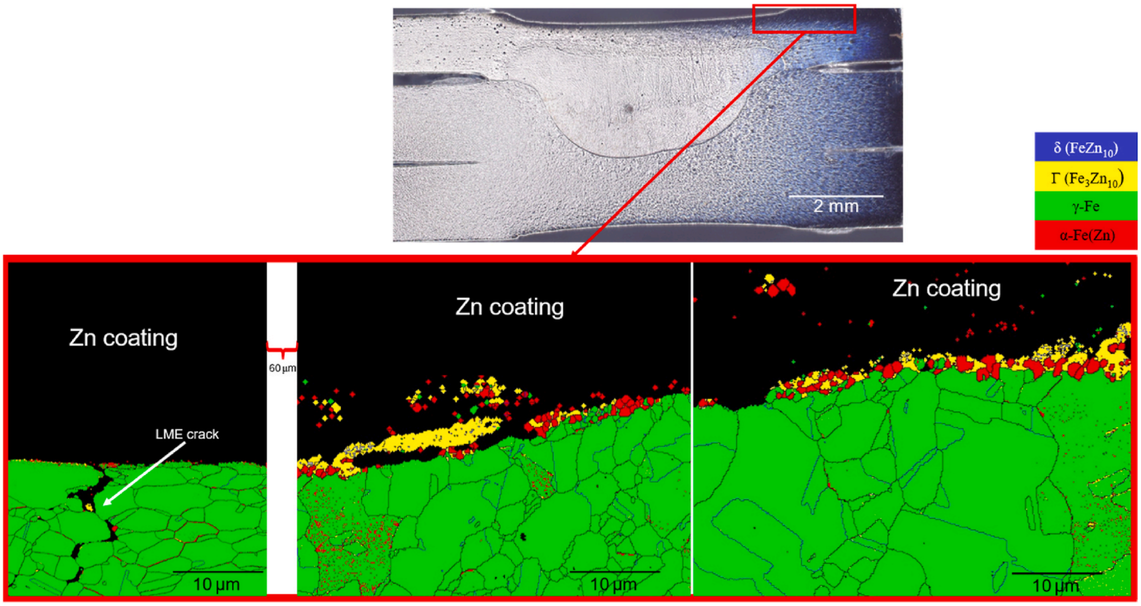

Fig. 12. EBSD phase map of RSW weld shoulder region at WT = 700 ms showing LME crack and IM formation.

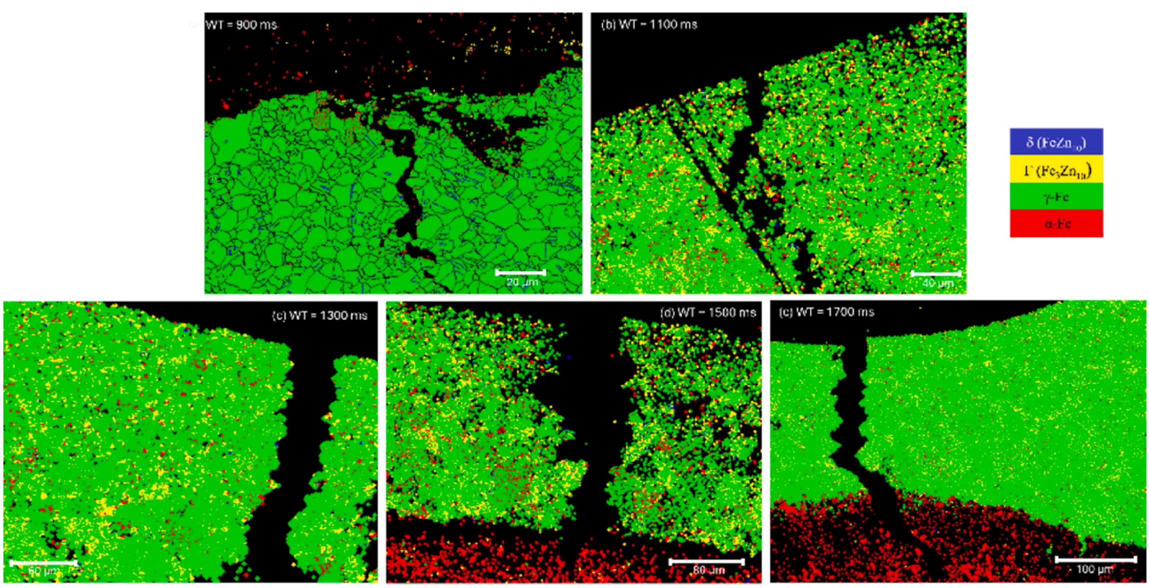

Fig. 13. EBSD phase maps of RSW samples at weld times of (a) 900 ms (b) 1100 ms (c) 1300 ms (d) 1500 ms (e) 1700 ms

calculated nugget areas.

At 500 ms, the simulation predicted incomplete fusion between the two DX54 sheets, which was consistent with the experimental cross-section. The difference between simulated and experimental nugget areas was 5.91%. At 700 ms, the model predicted a larger weld nugget extending into the bottom sheet, matching the micrograph, with a 4.87% difference in area. At 900 ms, the same trend was observed, with the nugget fully developed and a smaller difference of 1.69% between simulation and experiment.

The fusion zone boundary was selected as the validation reference because it provides a clear, unambiguous geometric feature for comparison. Although comparing the geometry of the HAZ would be more useful to validate the model, in fully austenitic TWIP steel the HAZ does not produce a sharp phase transformation boundary in cross-section or EBSD maps, making its geometry difficult to define reliably without introducing additional uncertainty.

3.3.2. *Temperature distribution analysis*

Fig. 15 shows the temperature distribution predicted by the FEA simulation across the weld cross-sections at weld times of 500 ms, 700 ms, and 900 ms, corresponding to the end of the weld time stage when the peak temperature is reached. Four points, A, B, C, and D, located between 3.4 mm and 5 mm from the weld centre were selected for detailed temperature analysis. These positions correspond to the weld shoulder region, where Fe-Zn IMs were experimentally observed. Fig. 15 also shows the temperature evolution at these points throughout the weld cycle.

At a weld time of 500 ms, the simulation shows that location D reaches a peak temperature of 470 °C. Locations C reaches a peak temperature of 645 °C and B reaches 816 °C. The peak temperature at Location A is 882 °C. At a weld time of 700 ms, location D reaches at peak temperature of 587 °C. Locations C and B reach peak temperatures of 771 °C and 930 °C, respectively, while location A reaches 980 °C. Locations A and B reach a temperature above the boiling point of Zn. At

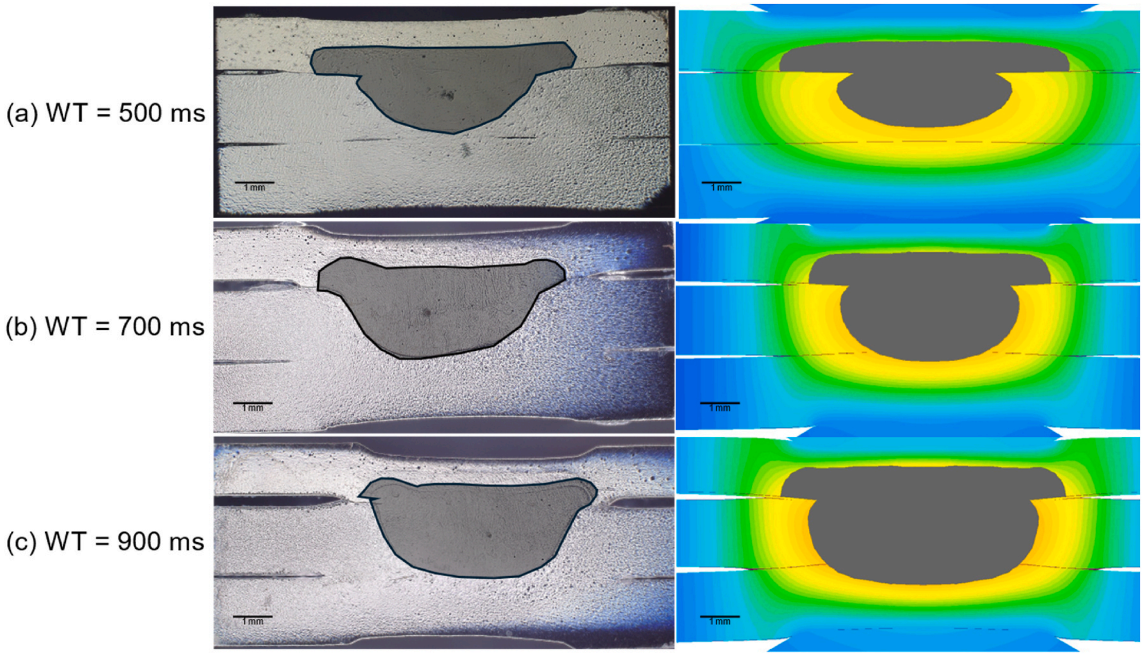

Fig. 14. Comparison of weld nugget geometry between RSW cross-sections and FEA simulations at weld times of (a) 500 ms (b) 700 ms (c) 900 ms

Table 6
Comparison of weld nugget area between RSW cross-section and FEA simulation.

Average weld nugget area from RSW sample (mm^2)	Weld nugget area from FEA simulation (mm^2)
6.52 ± 0.23	6.93
9.57 ± 0.38	10.06
10.43 ± 0.42	10.61

a weld time of 900 ms, locations A, B, C and reach peak temperatures of 1067 °C, 1015 °C, 875 °C and 675 °C respectively.

4. Discussion

In this study, all welding parameters were kept constant except for weld time to characterize the development of the Fe-Zn interface. Increasing weld time increases the temperature in the nugget and shoulder regions, which directly affects the formation of IMs, infiltration of Zn in the steel GBs, and the initiation and propagation of LME cracks

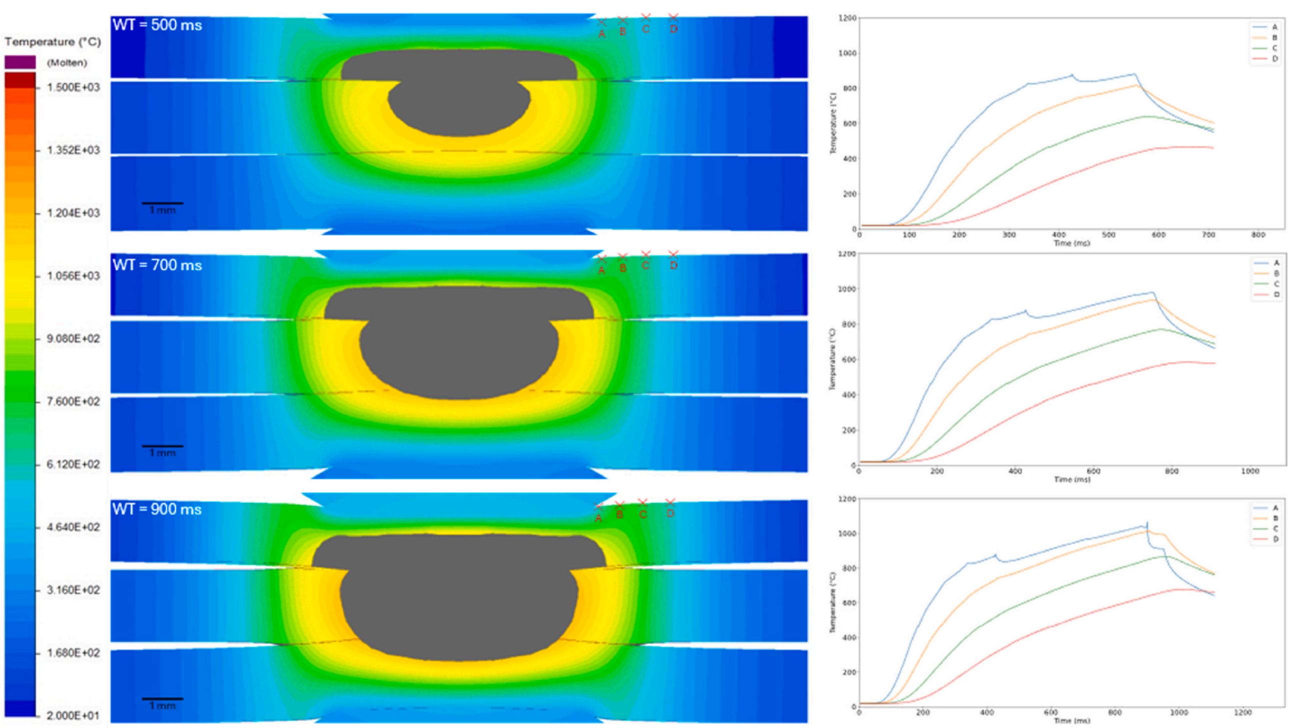

Fig. 15. Temperature distribution during RSW at weld times of 500 ms, 700 ms and 900 ms

[28,30]. An FEA model was developed on SORPAS to replicate RSW conditions. The FEA model accurately reproduces RSW conditions based on the comparison between the simulated and experimental weld nugget areas and nugget geometry. The differences in calculated nugget areas could be a result of loss of material from the cross-section during sample preparation or cutting.

When the temperature in the weld region exceeds 419 °C, Zn begins to melt. The applied electrode force pushes liquid Zn from the electrode-steel interface onto the weld shoulder [7]. At the lowest weld time of 300 ms, the Fe-Zn interface at the weld shoulder does not form IM layers. Some Al segregation at the interface is observed. Although not characterized by EBSD, this Al rich region is consistent with Al segregation at the Fe-Zn interface reported in galvanized steels [24–26]. At a weld time of 500 ms, the temperature at the weld shoulder region (locations C and D from Fig. 15) are between 470 °C and 650 °C, as calculated by the FEA model. Locations A and B exceeds 800 °C, above the stability limit for IMs. According to the Fe-Zn phase diagram, δ transforms to Γ and liquid Zn at 660 °C and Γ becomes α and liquid Zn at 782 °C [35,36]. These peritectic reactions results in the layers of IM phases observed at the Fe-Zn interface at the weld shoulder. SEM-EDS, STEM, and EBSD characterization of the 500 ms sample showed the formation of δ, Γ/Γ1, and α-Fe(Zn) layers above the austenitic steel. The identification of α-Fe(Zn) within the Γ matrix has been debated, with different studies reaching different conclusions depending on the methods used. Bertolo et al. reported a similar interfacial phase but characterized it as Γ from spherical indexation analysis of EBSD data and the absence of an α-Fe peak in XRD spectra [37]. In contrast, the present results from SEM-EDS and STEM-EDS show compositions with Fe contents greater than 75 wt%, consistent with α-Fe(Zn). EBSD also indicated a BCC structure, further supporting this identification. The absence of α-Fe(Zn) peaks in XRD performed in the current study could be due to the limited penetration depth of X-rays in the weld shoulder, where excess Zn solidifies after being displaced from the electrode-steel interface. The calculated thickness of the Zn layer in the weld shoulder is between 15 and 25 μm, which is higher than the penetration depth of the characterization technique, which is roughly 10 μm [38]. The Fe-Zn phase diagram is used here to identify which phases are thermodynamically stable at the estimated local temperatures, not as a quantitative prediction of phase fractions. The non-equilibrium conditions of RSW mean that exact transformation temperatures will deviate from equilibrium values, and the spatial distribution and amount of each phase will be governed by local kinetics.

Several other studies have also reported α-Fe(Zn) forming within a Γ matrix immediately above the austenitic steel, in agreement with the Fe-Zn phase diagram [39], which permits α-Fe(Zn) as a stable phase under these conditions [8,22,27,35]. EDS analysis also indicates that α-Fe(Zn) is enriched in Al compared to both the surrounding IMs and the bulk TWIP steel, while also showing a depletion in Mn. This partitioning behaviour suggests that Al is preferentially stabilized in the Fe-rich α-Fe (Zn) phase. According to Lee et al., an Al-rich layer typically forms between the Zn coating and the steel, acting as a barrier for Zn penetration. When welding temperatures and stresses cause the Al oxide barrier to break down, IMs can form, but the Al originating from the oxide layer does not diffuse far due to limited mobility [8]. Al is a ferrite stabilizer [40], and Mn in an austenite stabilizer [41]. During RSW, in regions where Al weight percentage is higher (1.85 wt% compared to 0.72 wt%) and Mn concentration is lower (2.48 wt% compared to ~17 wt%) than in the bulk TWIP steel, it becomes thermodynamically favourable for α-Fe(Zn) to form. This explains the observed Al enrichment and Mn depletion in α-Fe(Zn), as well as its stability at the Fe-Zn interface under welding conditions. It is also important to note that the EDS line scan profiles of Fe and Zn at the interface collected in the present study closely matched the results by other studies discussed in this section.

At WT = 700 ms, LME cracks initiate at the weld shoulder, but IMs are not present near the crack opening. Unlike the continuous chain of IM phases observed at WT = 500 ms, these IM layers at WT = 700 ms are broken and discontinuous. At a weld time of 700 ms, Fig. 15 from the FEA simulation shows the temperature at locations A and B exceed the boiling temperature of Zn. Location C reaches 771 °C which is almost at the maximum temperature of α-Fe(Zn) formation. This predicts a partially formed and discontinuous IM layer, consistent with the experimental observation of fragmented Fe-Zn layers shown in Fig. 12. At a weld time of 900 ms, locations A, B, and C all reach temperatures above 800 °C, too high for Fe-Zn IM stability. These conditions correspond to the absence of IMs and the appearance of LME cracks in the experimental samples. Crack openings provide escape paths for liquid Zn from the weld shoulder [17,19,42]. As a result, once cracks have initiated, the conditions are no longer favourable for stable intermetallic layers to form. At weld times between 900 ms and 1700 ms, results show that local temperatures at the weld shoulder exceed the stability range of Fe-Zn IMs. EBSD analysis confirms that no Fe-Zn IM phases are present at these weld times, while LME cracks are observed in all samples. The absence of δ, Γ, Γ_1 and α-Fe(Zn) phases indicate that the shoulder region experiences temperatures above ~800 °C - above the upper stability limit for Fe-Zn IMs. The LME cracks at weld times of 1500 ms and 1700 ms grow into the martensitic weld fusion zone. The progressive increase in crack depth and width from 900 ms to 1700 ms indicates that continued heating enhances liquid Zn penetration along GBs under tensile stress. This suggests that once IMs break down, liquid Zn can penetrate through the austenitic GBs and diffuse through the steel, propagating the LME crack [43]. It should be noted that all characterization was performed on samples cooled to room temperature. The phases observed are therefore affected by both heating and cooling, rather than the peak temperature microstructure alone. During cooling, liquid Zn re-solidifies and the local temperature passes back through the IM stability windows, which may result in additional phase transformations.

The findings of this study point to several directions for future work. The formation of α-Fe(Zn) is promoted by Al and suppressed by Mn, suggesting that steel composition and Zn coating chemistry could be tailored to encourage this barrier layer to form during RSW. Studying the effect of these alloying elements and coating composition could provide a route to reducing LME susceptibility. The effect of these IM layers on the mechanical properties of the weld joint is also worth investigating. Finally, the approach used here - isolating a single RSW parameter and characterising its effect on the Fe-Zn interface and LME - can be repeated for other parameters such as welding current, electrode force, and hold time to build a more complete understanding of how each one affects LME crack initiation.

4.1. Conclusions

This study characterizes the evolution of the Fe-Zn interface during RSW as a function of weld time, providing experimental snapshots of the interface before IM formation, during IM formation, at crack initiation, and during crack propagation - a sequence that has not been reported previously under actual RSW conditions. The combination of high resolution characterisation and FEA temperature modelling at LME crack locations to explain Fe-Zn interface behaviour during LME in RSW has not been reported previously.

At a weld time of 300 ms, the Zn coating remained intact and no IMs were observed. At 500 ms, δ, Γ, and α-Fe(Zn) phases formed as continuous layers at the weld shoulder. The α-Fe(Zn) phase was confirmed by SEM-EDS, STEM-EDS, and EBSD, showing Al enrichment and Mn depletion. At 700 ms, cracks initiated at the weld shoulder. IMs were absent at the crack opening but appeared as discontinuous and fragmented layers farther from the weld centre. Between 900 ms and 1700 ms, crack width and depth increased, and no IMs were present at the interface.

The FEA model, validated by comparison of simulated and experimental weld nugget areas, was used to analyse temperature distribution during welding. Simulations showed that at 500 ms, shoulder temperatures at selected locations matched the stability range for δ, Γ, Γ_1, and α-Fe(Zn), supporting the formation of continuous IM layers. At 700 ms, higher local temperatures predicted partial IM stability, consistent with fragmented layers observed experimentally. At 900 ms, temperatures exceeded the IM stability range, corresponding to conditions favourable for LME crack formation.

Overall, the combined experimental and simulation results show that Fe-Zn IM formation occurs before LME crack initiation and that increasing weld time leads to IM breakdown as local temperatures exceed their stability range. The validated FEA model provides a reliable method to link thermal conditions with interfacial reactions during RSW of TWIP steel.

CRediT authorship contribution statement

Gautham Mahadevan: Conceptualization, Data curation, Formal analysis, Investigation, Methodology, Validation, Writing – original draft. **Virginia Bertolo:** Conceptualization, Methodology, Writing – review & editing. **Soheil Sabooni:** Conceptualization, Methodology, Writing – review & editing. **He Gao:** Software, Validation, Writing – review & editing. **Vera Popovich:** Conceptualization, Supervision, Writing – review & editing. **Leo A.I. Kestens:** Conceptualization, Supervision, Writing – review & editing. **Marcel Hermans:** Conceptualization, Supervision, Validation, Writing – review & editing.

Declaration of competing interest

The authors declare the following financial interests/personal relationships which may be considered as potential competing interests: Gautham Mahadevan reports financial support was provided by Dutch Research Council. If there are other authors, they declare that they have no known competing financial interests or personal relationships that could have appeared to influence the work reported in this paper.

Acknowledgements

This publication is part of the project N19010 in the Partnership Program of the Materials Innovation Institute M2i framework, which is partly financed by the Dutch Research Council (NWO) and the partners Tata Steel and AutomotiveNL. We acknowledge Kees Kwakernaak from TU Delft for the help with the use of the SEM, EDS and EBSD equipment and Richard Huizenga for his assistance with XRD. We also acknowledge Vitaliy Bliznuk for his assistance in STEM characterization and the Welding and Joining Knowledge Group at Tata Steel Netherlands for providing the facilities to perform RSW tests.

Data availability

Data will be made available on request.

References

[1] A. Candela, G. Sandrini, M. Gadola, D. Chindamo, P. Magri, Lightweighting in the automotive industry as a measure for energy efficiency: review of the main materials and methods, Heliyon 10 (8) (2024 Apr 30) e29728, https://doi.org/10.1016/j.heliyon.2024.e29728.
[2] J.E. Norkett, M.D. Dickey, V.M. Miller, A review of liquid metal embrittlement: cracking open the disparate mechanisms, Metall. Mater. Trans. A 52 (6) (2021 Jun 1) 2158–2172, https://doi.org/10.1007/s11661-021-06256-y.
[3] T.B. Hilditch, T. de Souza, P.D. Hodgson, 2 - Properties and automotive applications of advanced high-strength steels (AHSS), in: M. Shome, M. Tumuluru (Eds.), Welding and Joining of Advanced High Strength Steels (AHSS) [Internet], Woodhead Publishing, 2015, pp. 9–28, https://doi.org/10.1016/B978-0-85709-436-0.00002-3. https://www.sciencedirect.com/science/article/pii/B9780857094360000023. (Accessed 6 July 2022).
[4] R. Kuziak, R. Kawalla, S. Waengler, Advanced high strength steels for automotive industry, Arch. Civ. Mech. Eng. 8 (2) (2008 Jan 1) 103–117, https://doi.org/10.1016/S1644-9665(12)60197-6.
[5] H. Zhang, J. Senkara, Resistance Welding: Fundamentals and Applications, CRC Press, Boca Raton, 2005, p. 444, https://doi.org/10.1201/b12507.
[6] J. Barthelmie, A. Schram, V. Wesling, Liquid metal embrittlement in resistance spot welding and hot tensile tests of surface-refined TWIP steels, IOP Conf. Ser. Mater. Sci. Eng. 118 (2016 Mar) 012002, https://doi.org/10.1088/1757-899X/118/1/012002.
[7] D. Bhattacharya, Liquid metal embrittlement during resistance spot welding of Zn-coated high-strength steels, Mater. Sci. Technol. 34 (15) (2018 Oct 13) 1809–1829, https://doi.org/10.1080/02670836.2018.1461595.
[8] H. Lee, M.C. Jo, S.S. Sohn, S.H. Kim, T. Song, S.K. Kim, et al., Microstructural evolution of liquid metal embrittlement in resistance-spot-welded galvanized TWinning-Induced plasticity (TWIP) steel sheets, Mater. Charact. 147 (2019 Jan 1) 233–241, https://doi.org/10.1016/j.matchar.2018.11.008.
[9] C. Béal, Mechanical Behaviour of a New Automotive High Manganese TWIP Steel in the Presence of Liquid Zinc [Theses], INSA de Lyon, 2011 [Internet], https://tel.archives-ouvertes.fr/tel-00679521. (Accessed 9 August 2022).
[10] C. Beal, X. Kleber, D. Fabregue, M. Bouzekri, Embrittlement of a zinc coated high manganese TWIP steel, Mater Sci Eng A 543 (2012 May 1) 76–83, https://doi.org/10.1016/j.msea.2012.02.049.
[11] S.H. Hong, J.H. Kang, D. Kim, S.J. Kim, Si effect on Zn-assisted liquid metal embrittlement in Zn-coated TWIP steels: Importance of Fe-Zn alloying reaction, Surf. Coat. Technol. 393 (2020 Jul 15) 125809, https://doi.org/10.1016/j.surfcoat.2020.125809.
[12] H. Kang, L. Cho, C. Lee, B.C. De Cooman, Zn penetration in liquid metal embrittled TWIP steel, Metall. Mater. Trans. A 47 (6) (2016 Jun 1) 2885–2905, https://doi.org/10.1007/s11661-016-3475-x.
[13] C. DiGiovanni, A. Ghatei Kalashami, E. Biro, N.Y. Zhou, Liquid metal embrittlement transport mechanism in the Fe/Zn system: Stress-assisted diffusion, Materialia 18 (2021 Aug 1) 101153, https://doi.org/10.1016/j.mtla.2021.101153.
[14] E.E. Glickman, Dissolution condensation mechanism of stress corrosion cracking in liquid metals: driving force and crack kinetics, Metall. Mater. Trans. A 42 (2) (2011 Feb 1) 250–266, https://doi.org/10.1007/s11661-010-0429-6.
[15] E.E. Glickman, Grain boundary grooving accelerated by local plasticity as a possible mechanism of liquid metal embrittlement, Interface Sci. 11 (4) (2003 Oct 1) 451–459, https://doi.org/10.1023/A:1026100112248.
[16] V.V. Popovich, I.G. Dmukhovskaya, Rebinder effect in the fracture of Armco iron in liquid metals, Sov Mater Sci Transl Fiz-Khimicheskaya Mekhanika Mater Acad Sci Ukr SSR 14 (4) (1978 Jul 1) 365–370, https://doi.org/10.1007/BF01154711.
[17] W. Dong, H. Pan, M. Lei, K. Ding, Y. Gao, Zn penetration and its coupled interaction with the grain boundary during the resistance spot welding of the QP980 steel, Scr. Mater. 218 (2022), https://doi.org/10.1016/j.scriptamat.2022.114832. Located at: Scopus.
[18] Z. Ling, T. Chen, L. Kong, M. Wang, H. Pan, M. Lei, Liquid metal embrittlement cracking during resistance spot welding of galvanized Q&P980 steel, Metall Mater Trans A. 50 (11) (2019 Nov 1) 5128–5142, https://doi.org/10.1007/s11661-019-05388-6.
[19] J.S. Dohie, J.R. Cahoon, W.F. Caley, The grain-boundary diffusion of Zn in α-Fe, J. Phase Equilibria Diffus. 28 (4) (2007 Aug 1) 322–327, https://doi.org/10.1007/s11669-007-9093-y.
[20] Y. Ikeda, H.C. Ni, A. Chakraborty, H. Ghassemi-Armaki, J.M. Zuo, R.D. Kamachali, et al., Segregation-induced grain-boundary precipitation during early stages of liquid-metal embrittlement of an advanced high-strength steel, Acta Mater. 259 (2023 Oct 15) 119243, https://doi.org/10.1016/j.actamat.2023.119243.
[21] M.H. Razmpoosh, Investigation of liquid-metal-embrittlement crack-path: Role of Grain Boundaries and Responsible Mechanism [Internet], University of Waterloo, 2020. https://uwspace.uwaterloo.ca/handle/10012/16072. (Accessed 4 August 2022).
[22] S.P. Murugan, J. Kim, J. Kim, Y. Wan, C. Lee, J.B. Jeon, et al., Role of liquid Zn and α-Fe(Zn) on liquid metal embrittlement of medium Mn steel: an ex-situ microstructural analysis of galvannealed coating during high temperature tensile test, Surf. Coat. Technol. 398 (2020 Sep 25) 126069, https://doi.org/10.1016/j.surfcoat.2020.126069.
[23] A. Ghatei-Kalashami, M.S. Khan, F. Goodwin, Y.N. Zhou, Investigating the mechanism of zinc-induced liquid metal embrittlement crack initiation in austenitic microstructure, J. Mater. Sci. (2023 Oct 17), https://doi.org/10.1007/s10853-023-08963-w.
[24] Jr. S. Feliu, V. Barranco, XPS study of the surface chemistry of conventional hot-dip galvanised pure Zn, galvanneal and Zn-Al alloy coatings on steel, Acta Mater. 51 (18) (2003) 5413–5424, https://doi.org/10.1016/S1359-6454(03)00408-7. Located at: Scopus.
[25] H.E. Biber, Scanning auger microprobe study of hot-dipped regular-spangle galvanized steel: part I. surface composition of As-produced sheet, Metall. Trans. A 19 (6) (1988) 1603–1608, https://doi.org/10.1007/BF02674035. Located at: Scopus.
[26] A. Rodnyansky, Y.J. Warburton, L.D. Hanke, Segregation in hot-dipped galvanized steel, Surf. Interface Anal. 29 (3) (2000) 215–220, https://doi.org/10.1002/(SICI)1096-9918(200003)29:3<215::AID-SIA703>3.0.CO;2-X. Located at: Scopus.
[27] Y. Ikeda, R. Yuan, A. Chakraborty, H. Ghassemi-Armaki, J.M. Zuo, R. Maaß, Early stages of liquid-metal embrittlement in an advanced high-strength steel, Mater Today Adv 13 (2022 Mar 1) 100196, https://doi.org/10.1016/j.mtadv.2021.100196.
[28] C. Böhne, G. Meschut, M. Biegler, M. Rethmeier, Avoidance of liquid metal embrittlement during resistance spot welding by heat input dependent hold time adaption, Sci. Technol. Weld. Join. 25 (7) (2020 Oct 1) 617–624, https://doi.org/10.1080/13621718.2020.1795585.
[29] S. Dwibedi, B. Kumar, S.R. Bhoi, S.R. Tripathy, S. Pattanaik, S. Prasad, et al., To investigate the influence of weld time on joint characteristics of Hastelloy X weldments fabricated by RSW process, Mater. Today Proc. (2020 Jan 1)

2763–2769, https://doi.org/10.1016/j.matpr.2020.02.576, 10th International Conference of Materials Processing and Characterization26.

[30] H. Moshayedi, I. Sattari-Far, Resistance spot welding and the effects of welding time and current on residual stresses, J. Mater. Process. Technol. 214 (11) (2014 Nov 1) 2545–2552, https://doi.org/10.1016/j.jmatprotec.2014.05.008.

[31] H. Long, Y. Hu, X. Jin, J. Shao, H. Zhu, Effect of holding time on microstructure and mechanical properties of resistance spot welds between low carbon steel and advanced high strength steel, Comput. Mater. Sci. 117 (2016 May 1) 556–563, https://doi.org/10.1016/j.commatsci.2016.01.011.

[32] S.P. Murugan, V. Vijayan, C. Ji, Y.D. Park, Four types of LME cracks in RSW of Zn-coated AHSS, Weld. J. 99 (3) (2020) 75s–92s.

[33] M. Krenn, Characterization of Fe-Zn intermetallic compounds via advanced Electron microscopy [VerfasserIn] Characterization of Fe-Zn Intermetallic Compounds via Advanced Electron Microscopy [Internet]. Linz, https://permalink.obvsg.at/AC17469731, 2025.

[34] N. Saunders, U.K.Z. Guo, X. Li, A.P. Miodownik, JPh Schillé, Using JMatPro to model materials properties and behavior, JOM 55 (12) (2003 Dec 1) 60–65, https://doi.org/10.1007/s11837-003-0013-2.

[35] H. Inui, N.L. Okamoto, S. Yamaguchi, Crystal structures and mechanical properties of Fe–Zn intermetallic compounds formed in the coating layer of galvannealed steels, ISIJ Int. 58 (9) (2018) 1550–1561, https://doi.org/10.2355/isijinternational.ISIJINT-2018-066.

[36] J.U. Kim, S.P. Murugan, J.S. Kim, W. Yook, C.Y. Lee, C. Ji, et al., Liquid metal embrittlement during the resistance spot welding of galvannealed steels: synergy of liquid Zn, α-Fe(Zn) and tensile stress, Sci. Technol. Weld. Join. 26 (3) (2021 Apr 1) 196–204, https://doi.org/10.1080/13621718.2021.1880816.

[37] V. Bertolo, G. Mahadevan, R.H. Petrov, V. Popovich, The role of microstructure in crack growth during liquid metal embrittlement of Zn-galvanised TWIP steel, J. Mater. Res. Technol. 38 (2025 Sep 1) 2569–2577, https://doi.org/10.1016/j.jmrt.2025.08.097.

[38] Y. Waseda, E. Matsubara, K. Shinoda, X-Ray diffraction crystallography: introduction, examples and solved problems [Internet], Springer, Berlin, Heidelberg, 2011, https://doi.org/10.1007/978-3-642-16635-8. https://link.springer.com/10.1007/978-3-642-16635-8. (Accessed 7 November 2025).

[39] O.K. von Goldbeck, Fe—Zn Iron—Zinc, in: Goldbeck OK. von (Ed.), IRON—Binary Phase Diagrams [Internet], Springer, Berlin, Heidelberg, 1982, pp. 172–175, https://doi.org/10.1007/978-3-662-08024-5_79. (Accessed 7 November 2025).

[40] J. Cui, K. Li, Z. Yang, Z. Wu, Y. Wu, Investigation of effects of aluminum additions on microstructural evolution and mechanical properties of ultra-high strength and vanadium bearing dual-phase steels, J. Mater. Res. Technol. 31 (2024 Jul 1) 1117–1131, https://doi.org/10.1016/j.jmrt.2024.06.148.

[41] R.L. Klueh, P.J. Maziasz, E.H. Lee, Manganese as an austenite stabilizer in Fe Cr Mn C steels, Mater Sci Eng A 102 (1) (1988 Jun 1) 115–124, https://doi.org/10.1016/0025-5416(88)90539-3.

[42] R. Frappier, P. Paillard, R.L. Gall, T. Dupuy, Embrittlement of steels by liquid zinc: crack propagation after grain boundary wetting, Adv. Mater. Res. 922 (2014) 161–166. http://doi.org/10.4028/www.scientific.net/AMR.922.161.

[43] D. Bhattacharya, L. Cho, E. van der Aa, A. Pichler, N. Pottore, H. Ghassemi-Armaki, et al., Influence of the starting microstructure of an advanced high strength steel on the characteristics of Zn-Assisted liquid metal embrittlement, Mater Sci Eng A 804 (2021 Feb 15) 140391, https://doi.org/10.1016/j.msea.2020.140391.